

The Collisional and Photoionized Plasma in the Polarized NLS1 galaxy Mrk 1239

Margaret Z. Buhariwalla,¹★ Luigi C. Gallo,¹ J. Mao,^{2,3} S. Komossa,⁴ J. Jiang,⁵ A. Gonzalez,¹ and D. Grupe⁶

¹Department of Astronomy and Physics, Saint Mary's University, 923 Robie Street, Halifax, NS B3H 3C3, Canada

²Department of Astronomy, Tsinghua University, 30 Shuangqing Road, Beijing 100084, China

³Department of Physics, Hiroshima University, 1-3-1 Kagamiyama, Higashi-Hiroshima City, Hiroshima 739-8526, Japan

⁴Max-Planck-Institut für Radioastronomie, Auf dem Hügel 69, 53121, Bonn Germany

⁵Institute of Astronomy, University of Cambridge, Madingley Road, Cambridge CB3 0HA UK

⁶Department of Physics, Geology, and Engineering Technology Science Center, Northern Kentucky University, 1 Nunn Drive, Highland Heights, KY 41099

Accepted XXX. Received YYY; in original form ZZZ

ABSTRACT

Mrk 1239 is a highly polarized NLS1 in the optical band, whose 0.3 – 3 keV spectrum has remained remarkably consistent over more than two decades of observation. Previous analysis of this object suggested that the soft X-ray band was dominated by emission lines (collisionally and/or photoionized) from the distant host galaxy as the X-ray emission from the central engine was highly obscured. New *XMM-Newton* data of Mrk 1239 are presented here to investigate the soft X-ray band of this galaxy with high resolution. The first RGS spectra of this source reveal a plethora of ionized emission lines originating from two distinct plasmas, one collisionally ionized and the other photoionized at approximately equal brightness. The best fit model uses *APEC* and *XSTAR* grids to account for the collisionally ionized and photoionized components, respectively. The fit improves significantly if the photoionized material is allowed to outflow at $\approx 500 \text{ km s}^{-1}$, matching the outflow velocity of the forbidden O VII emission line. From constraints on the ionization and density of the photoionized material we can estimate the location of it to be no further than a few pc from the central source, around the outer radius of the torus, which is consistent with the O VII(*f*) emission line. Properties of the collisionally ionized plasma are consistent with star formation rate (SFR) of $\approx 3 \text{ M}_{\odot} \text{ yr}^{-1}$, which is comparable with several previous measurements of the SFR in this galaxy.

Key words: X-rays: galaxies – galaxies: star formation – galaxies: nuclei – galaxies: Seyfert

1 INTRODUCTION

Mrk 1239 is a Narrow Line Seyfert 1 galaxy (NLS1) located at a redshift of $z = 0.01993$ (Beers et al. 1995). The optical spectra of Mrk 1239 was first reported by Rafanelli & Bonoli (1984) and later used by Osterbrock & Pogge (1985) to define the subclass of galaxies known as NLS1s. They suggest a classification criterion for NLS1 to have $H\beta$ line widths less than 2000 km s^{-1} . This is now commonly adopted by the community (see Komossa 2008, for a complete review). These active galaxies are thought to be low mass counterparts of broad line Seyfert 1s (BLS1). They show intense X-ray variability on both long-term and rapid time scales (see Gallo 2018; Wilkins et al. 2017; Wilkins & Gallo 2015). These objects are seen through low column densities and often exhibit steep powerlaw continuum (Waddell & Gallo 2020) and strong soft excesses (Waddell et al. 2019).

Mrk 1239 is a radio quiet galaxy that shows evidence of non-stellar radio emission (Doi et al. 2015). This indicates the possible presence of a radio jet originating from the AGN in this galaxy. Mrk 1239 is also a highly polarized in the broad $H\alpha$ and $H\beta$ emission lines, along with the continuum (Pan et al. 2019, 2021). The high levels of polarization in Mrk 1239 have previously been observed by

Goodrich (1989) where Mrk 1239 was the highest polarized source in the sample. This suggests some amount of scattered emission in this source. Mrk 1239 is classified as a polar-scattered Seyfert 1 galaxy, meaning the line of sight is through the upper layers of the torus (Smith et al. 2004; Jiang et al. 2019). As well Goodrich (1989) found that the Balmer lines had a higher polarization than the forbidden [O III] lines. This is strong evidence that the sources of these emissions lines is physically distinct.

Mrk 1239 was first observed in X-ray using *ROSAT* where a steep photon index was found ($\Gamma \approx 3$, Rush & Malkan 1996; Jiang et al. 2021). Mrk 1239 was a serendipitous source in a 2001 observation by *XMM-Newton* and analysed by Grupe et al. (2004). They found the continuum was best fit using a powerlaw with two intrinsic absorbers: the first a direct, highly absorbed path and the second a less absorbed scattered path. They concluded that this was consistent with the distinct emitting/scattering regions found in Goodrich (1989). Finally, Grupe et al. (2004) found an excess of emission at 0.91 keV, which was attributed to a blend of the Ne IX triplet. However, the O VII triplet was not observed in the spectrum suggesting a super-solar ratio of Ne/O in Mrk 1239.

Mrk 1239 was revisited by Buhariwalla et al. (2020) with archival X-ray data from *Suzaku* and *NuSTAR*, obtained in the subsequent years since Grupe et al. (2004). With this broadband multi-epoch analysis some truly unique behaviour was revealed. First and fore-

★ E-mail: margaret.buhariwalla@smu.ca

most, across the 18 years of data analysed the shape and flux of the spectra below 3 keV remain remarkably similar. Meanwhile, the spectrum above 3 keV retained the characteristic NLS1 variability. This immediately indicated the presence of a strong absorbing feature that blotted out most of the emission from the central engine below 3 keV. The 0.91 keV feature was present in the 2007 *Suzaku* observation of Mrk 1239.

Continuum modelling of this source between 0.3 and 30 keV saw a ionized partial covering model compared to a blurred reflection model. The data were insufficient to significantly distinguish between the two models but their similarities proved to be more interesting. Both models required high levels of intrinsic absorption and both models required the presence of a collisionally ionized component to fit the spectrum below 3 keV. Buhariwalla et al. (2020) attributed this collisionally ionized emission (CIE) to the presence of star forming activity in this object. They proposed that the 0.91 keV feature found originally by Grupe et al. (2004) was not an overabundance of Ne, but a blend of Fe-L lines from the regions of star formation. Using a relationship between the $L_{2-10\text{ keV}}$ of the CIE and star formation rate (SFR) (Franceschini et al. 2003), the SFR of Mrk 1239 was found to be $\approx 4 - 6 M_{\odot} \text{ yr}^{-1}$. This is comparable with the SFR of $< 7.5 M_{\odot} \text{ yr}^{-1}$ measured using PAH signatures (Ruschel-Dutra et al. 2016), $\sim 3.5 M_{\odot} \text{ yr}^{-1}$ found using SED fitting (Gruppioni et al. 2016), and $\sim 2.1 M_{\odot} \text{ yr}^{-1}$ found using IR measurements (Smirnova-Pinchukova et al. 2022). To fully probe the soft band of this galaxy and determine the origin of the 0.91 keV feature conclusively deeper observations of Mrk 1239 were needed.

This paper presents the first high-resolution X-ray spectrum of Mrk 1239 in the 7 – 31 Å band with the *XMM-Newton* RGS spectra. Limited MOS/PN spectra of a deep observation of Mrk 1239 and a *Chandra* image is also presented. In Section 2, the observations and data reduction techniques are summarized. Section 3 examines the *Chandra* image, emission line identification, possible outflow velocities, plasma diagnostics and the possibility of a Ne/O and in Section 4 the spectra are analyzed. A discussion of the results is given in Section 5, and conclusions are drawn in Section 6.

2 OBSERVATIONS AND DATA REDUCTION

A snapshot observation of Mrk 1239 was taken on 2021-04-11 with *Chandra* as part of a sample study exploring dual AGN (Foord 2020). Several months later a deep observation of Mrk 1239 was taken on 2021-11-04 with *XMM-Newton* and *NuSTAR*, with each obtaining ≈ 100 ks of on source time. During the second half of the *NuSTAR* observation Mrk 1239 entered a flaring state. To fully explore all facets of this object analysis of the *NuSTAR* and broad band *XMM-Newton* data is relegated to a second paper. The data for analysis are listed in Table 1. This section describes the observations and data reduction.

2.1 *XMM-Newton*

Mrk 1239 was observed with *XMM-Newton* (Jansen et al. 2001) for 105 ks starting on November 4th 2021. The *XMM-Newton* Observation Data Files (ODF) were processed to produce calibrated event lists using the *XMM-Newton* Science Analysis System, SAS V17.0.0. The first order RGS data was extracted from the ODF using RGSPROC. Upon analysis of the light curve a background flaring event was seen within the first 15 ks. TABGTIGEN was used to filter all instances where the count s^{-1} was greater than or equal to 0.1. The spectra was then re-extracted using RGSPROC. RGS1 and

RGS2 were then combined using RGSCOMBINE, which produced a combined source spectra, background spectra, and response matrix. The source and background spectra were then optimally binned using FTGROUPPHA (Kaastra & Bleeker 2016), the spectra were loaded into XSPEC where the background was modelled. Fits were evaluated using Cash-statistics (C-stat, Cash 1979).

For the PN spectra an event list was created from the ODF using EPPROC. The lightcurve was generated using EVSELECT and used to examine for background flaring. The same flare seen in the RGS data was present in the PN data, thus TABGTIGEN was used to filter all times when the count s^{-1} were greater than or equal to 10. The spectra was also examined for pileup and was found to be satisfactory. The source spectra was extracted from a circular region 35" centred on Mrk 1239. A background region was extracted from a circular region with a radius of 50" on the same chip. RMFGEN and ARFGEN were used to generate response files for the observation.

2.2 *Chandra*

Mrk 1239 was observed with *Chandra* in April 2021 for 2.1 ks, and the data entered the archive in April 2022. The image was captured using *Chandra* ACIS-S instrument and the data was processed using CIAO 4.14¹. Initially a spectrum was extracted using DMEXTRACT. The spectrum was then loaded into SHERPA where a rough fit was obtained and saved over the energy region of interest, 0.2-2.0 keV. The spectral shape obtained by this rough fit was imputed in CHART² along with the nominal RA and DEC of the observation to generate a simulated PSF. The PSF was then projected in the detector plane using MARX via SIMULATE_PSF with a bin size of 1 pixel and a blur factor of 0.25. Next the image was exposure corrected using FLUXIMAGE, where an exposure corrected map centred around the brightest pixel in the image with a 600 pixel box, with bin size of 1 pixel. The image was extracted with a minimum energy of 0.2 keV, a maximum energy of 2 keV, and an effective energy of 1 keV. Finally the image was deconvolved with the PSF generated previously using ARESTORE with the Lucy-Richardson deconvolution algorithm and 100 iterations. The final image presented is smoothed using a Gaussian interpolation method.

3 ANALYSIS

3.1 Extended emission in 0.2-2 keV

The 2.1 ks image of Mrk 1239 taken with *Chandra* ACIS-S is presented in Figure 1. The radio contours are taken from Järvelä et al. (2022) and are based on JVLA observations centred at 5.2 GHz with a 2 GHz bandwidth. They give a sense of size and shape of the extended radio emission region.

Most of the soft X-ray emission originates from the very central region of the galaxy, suggesting at least part of it is originating from the AGN. Previous studies have indicated that there is star formation present within the central 400 pc of nucleus of Mrk 1239 (Ruschel-Dutra et al. 2016). This appears comparable to the scale of the extended soft X-ray emission in the *Chandra* image thus some of the soft emission seen in the central region may be the result of this star formation. There appears to be asymmetry extending to the Southeast quadrant of Mrk 1239. Detailed analysis is limited by the

¹ <https://cxc.cfa.harvard.edu/ciao/>

² <https://cxc.cfa.harvard.edu/ciao/PSFs/chart2/runchart.html>

(1)	(2)	(3)	(4)	(5)	(6)	(7)	(8)
Observatory	Observation ID	Instrument Name	Start date (yyyy-mm-dd)	Duration [s]	Exposure [s]	Counts	Energy range
<i>XMM-Newton</i>	0891070101	PN	2021-11-04	105000	79175	1512	0.2 – 2.0 keV
<i>XMM-Newton</i>		RGS	2021-11-04	105000	193963*	5660	7 – 31 Å
<i>Chandra</i>	23693	ACIS-S	2021-04-11	2100	2021	50	0.2 – 2 keV

Table 1. Observations log for Mrk 1239. The observations and instruments used for analysis are listed in column (1). The observation ID and labels used in this work are given in columns (2) and (3), respectively. The start date of each observation is given in column (4). The duration of each observation, total exposure time and total counts for each observation are given in columns (5), (6), and (7), respectively. The energy/wavelength each observation were fit over is given in column (8). *For RGS the combined exposure and counts for RGS1 and RGS2 are reported.

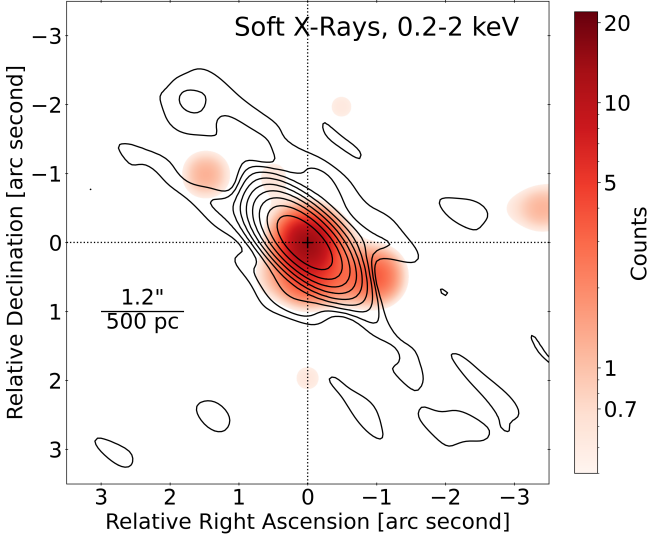


Figure 1. Snap-shot image of Mrk 1239 taken with *Chandra*-ACIS-S instrument. The JVLA 5.2 GHz radio contours are provided by Järvelä et al. (2022).

short exposure time, and deeper observations would be needed to determine the exact location of the soft emission.

3.2 Emission Line Search

Mrk 1239 is not a particularly bright source, as such we cannot confidently identify the continuum level. Instead, we observe emission lines poking above the background (Figure 2 top panel). Due to the high background level it was imperative to find all regions where the data were significant over the background. This was achieved by modelling the background (see Figure 2 middle panel) and applying the model to the source spectrum.

A Gaussian profile with a width of $\sigma = 0.01$ Å was then applied beginning at 7 Å. The normalization was stepped through twenty values space evenly in log space between 5×10^{-7} and 5×10^{-5} photons/cm²/s using the *xspec* command *STEPPAR*. For each normalization step the best fit improvement was recorded. When complete the Gaussian profile was moved 0.005 Å (an order of magnitude finer than the instrument resolution of RGS) and the process was repeated, covering all wavelengths between 7 and 35 Å. This allowed for the spectra to be oversampled and provide a clear picture of where the source was detected above the background.

The maximum fit improvement was taken at each wavelength regardless of the normalisation required. The maximum fit improvement (Max ΔC) verse wavelength was plotted as a visualization tool to more clearly identify the locations of possible lines. This max fit

improvement line can be seen in the bottom panel of Figure 2. Forty-five line candidates were identified, all having a fit improvement of at least $\Delta C = 5$.

Next a Gaussian profile with a width of 0.01 Å was applied for each of the 45 line candidates, the normalizations were fit and subsequently frozen. The error on the line energies was then calculated using the *xspec* error command. The uncertainty in the line energy, plus an outflow correction factor (see Sec. 3.3), was used as the search range up until a maximum search range of 0.1 Å. With the line wavelength and search range imputed in AtomDB, the most probable line candidate was identified.

Forty line candidates were recovered, they are detailed in Table 3.2, while the data and the search line are shown in Figure 3. No radiative recombination continuum (RRC) features were identified through this process as a continuum was not confidently identified. The search was preformed over the wavelength range 7 – 35 Å, however lines were only significantly detected between 9 – 26 Å.

3.3 O VII Outflow velocity

While examining possible line candidates it was found that several emission features exhibited slight blue shifts in their line energy. Figure 4 shows the velocity profile of the forbidden O VII line. This was the strongest isolated line. The rest frame wavelength of this line is $22.06^{+0.01}_{-0.02}$ Å while the laboratory measurement is 22.098 Å. The resultant outflow velocity is -500^{+100}_{-300} km s⁻¹. The measured velocity is comparable to other outflows in Seyfert galaxies (see NGC 5548 Mao et al. 2018; NGC 4151 Armentrout et al. 2007; NGC 1068 Grafton-Waters et al. 2021). Outflow velocities from other emission lines were not as well constrained. As well, Mrk 1239 does show evidence for an outflow in the [O III] line of ~ 2000 km s⁻¹, located between 10-100 pc of the SMBH (Pan et al. 2021).

3.4 Plasma Diagnostics

He-like ions produce very specific emission features dependant on the density, temperature and processes by which the atoms were ionized. A common method for determining the density and temperature of the emitting plasma is by using the *G* and *R* ratios defined in Equations 1 and 2. For these diagnostics *z* is the forbidden line (*f*), *x* + *y* are the inter-combination lines (*i*), and *w* is the resonance line (*r*) (Porquet & Dubau 2000).

$$R = \frac{z}{x + y} = \frac{f}{i} \quad (1)$$

$$G = \frac{x + y + z}{w} = \frac{f + i}{r} \quad (2)$$

For Mrk 1239 only the He-like triplet of O VII is strongly detected. There is some evidence of Mg XI and Ne IX, but the O VII triplet

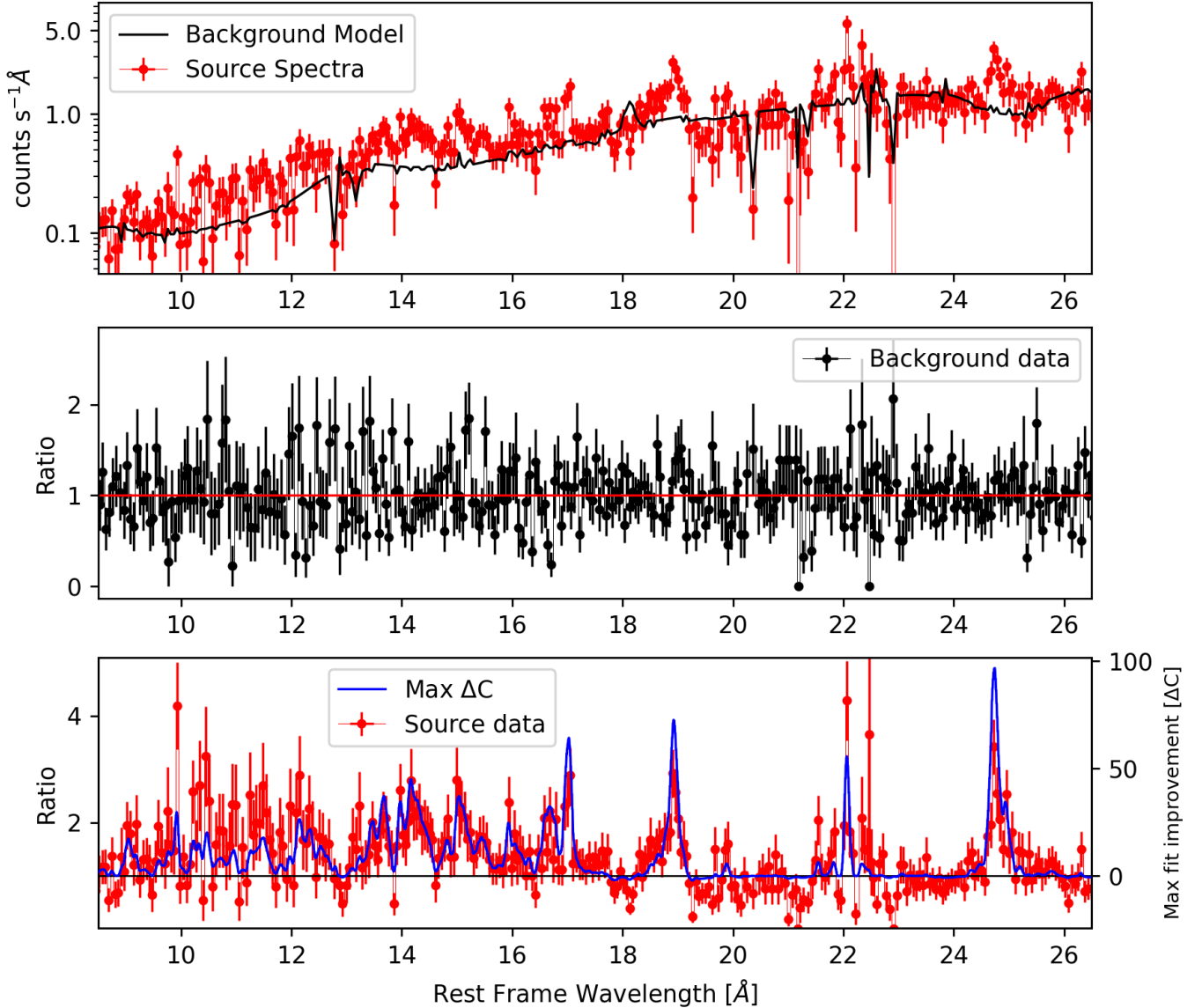


Figure 2. *Top panel:* the RGS spectrum is shown in red, while the background model is shown in black. *Middle panel:* the ratio of the background model to the background data. *Bottom panel:* The ratio of the source data to the background model is shown in red. In blue is the maximum fit improvement (Max ΔC) found by the line search (right axis). The black line is at a ratio of 1 on the left axis and at a maximum fit improvement of 0 C-stat on the right axis. The blue line details where the source is above the background.

is clearly seen. This may be due to the blend of lines around Mg and Ne originating from other species and the relative lack of other lines around the O VII triplet. For this work both the O VII and Ne IX He-like triplets are explored.

Due to the weak intercombination lines in this spectra it was difficult to ascertain the uncertainties of the G and R ratios. To overcome this we implemented a model in *xspec* so that the values and their uncertainties might be directly outputted. This was achieved by re-writing the G and R ratio such that f and r could be expressed in terms of G , R and i . To do this the first step is a simple rearrangement of the R ratio:

$$f = R \times i. \quad (3)$$

Next the G ratio:

$$r = \frac{f + i}{G}. \quad (4)$$

Substituting in what we know about f from Equation 3;

$$r = \frac{R \times i + i}{G} \quad (5)$$

The subtlety of this method is revealed when we consider how to implement it directly in *xspec*. The expression would be: $(\text{constant}_G \times \text{zagauss}_r + \text{zagauss}_i + \text{constant}_R \times \text{zagauss}_f)$, where the subscripts denote the parameter the component represents. The correct normalization for zagauss_r is $\frac{R \times i + i}{G}$ but the component is multiplied by G therefore the normalization must be $\frac{R \times i + i}{G^2}$. Similarly the correct normalization on f is $R \times i$, because the component is already multiplied by R we simply link the two components. This

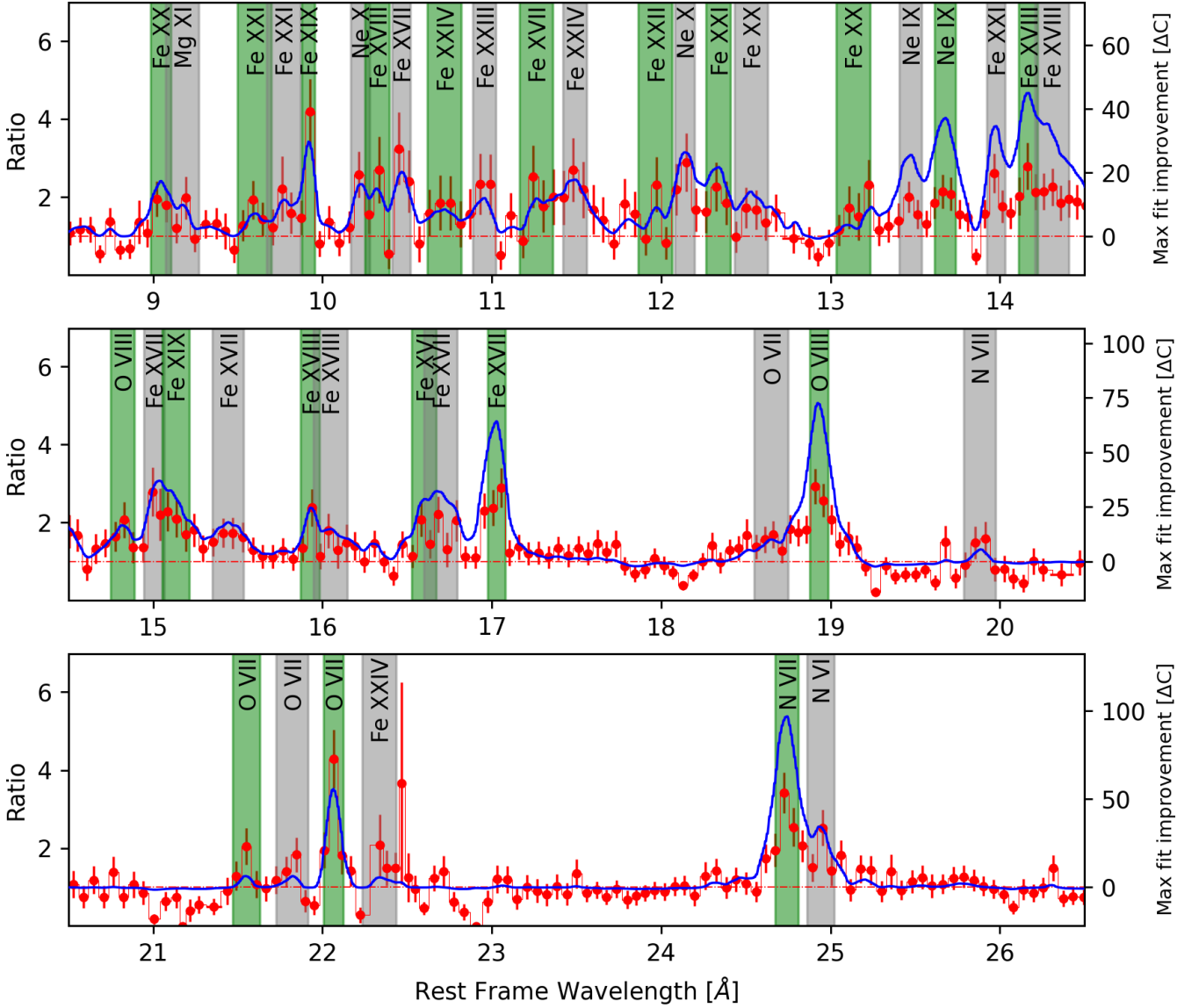


Figure 3. Results of the blind line search with candidate lines labelled. Red denotes the ratio of the RGS data to the background model. The blue line is the maximum fit improvement (Max ΔC) at any wavelength. The shaded green and gray regions denote the search radius used in AtomDB and the label given in each shaded region is the most probable line ID that produced that emission feature. The different colour bands are simply used to distinguish nearby lines. As a reminder, anywhere the RGS data drops below 1 is a region where the background was above the source.

leaves G , R and i free to fit the triplet. The added complication here is the outflow we see on $O\text{ VII}(f)$, thus we have an additional component, v_{MSHIFT} , to account for the outflow. The outflow velocities are linked for the r , i and f lines. The G and R ratio for $O\text{ VII}$ and Ne IX as well as their outflow velocities are displayed in Table 3.4.

Comparing the strength of the resonance line to the strength of the $\text{Ly}\alpha$ line reveals that the ratio of H-like/He-like atoms for both the $O\text{ VII}$ and Ne IX atoms is of order unity. This allows us to use the G ratio to find a temperature of the order 10^6 K (Porquet & Dubau 2000). This estimation is not without its caveats, as it assumes that the regions where the H-like ions are formed is the same as where the He-like ions are formed which is not necessarily the case according to Porquet & Dubau (2000).

Due to the weak intercombination line in both triplets the R ratio was not well constrained and we can only provide lower limits on

it and the density estimations. Comparing the calculated values to the $R(n_e)$ curves produced by Porquet & Dubau (2000) we gain limited information. For $O\text{ VII}$, which has $R > 2.5$, this tells us that the plasma that produced these emission lines has a density less than 10^{11} cm^{-3} . The plasma that produced the Ne IX emission lines has a density less than 10^{12} cm^{-3} . Moreover, the outflow velocity of the $O\text{ VII}$ triplet is consistent with the velocities reported in Section 3.3. The outflow velocity of the Ne IX triplet agrees with that of the $O\text{ VII}$ triplet, and it also agrees with being at rest with the galaxy as a whole.

The final piece of information we can deduce from the He-like ions is from the relative strength of the resonance line. In purely photoionized plasmas the resonance line is weaker compared to the intercombination and forbidden lines. Whereas, in mixed plasmas, containing both photoionized and collisionally ionized emission, the resonance line is relatively strong. If we look at the $O\text{ VII}$ triplet we

(1)	(2)	(3)	(4)	(5)
Ion ID	Observed wavelength [Å]	Search range [Å]	Rest wavelength [Å]	ΔC
Fe xx	9.05 ± 0.04	0.059	9.066	17
Mg xi	9.2 ± 0.2	0.100	9.169	10
Fe xxi	9.60 ± 0.08	0.100	9.504	7
Fe xxi	9.8 ± 0.2	0.100	9.819	11
Fe xix	$9.92^{+0.01}_{-0.02}$	0.038	9.945	30
Ne x	10.22 ± 0.04	0.057	10.238	16
Fe xviii*	$10.32^{+0.06}_{-0.05}$	0.072	10.360	15
Fe xvii	$10.47^{+0.03}_{-0.04}$	0.053	10.504	20
Fe xxiv	$10.7^{+0.1}_{-0.2}$	0.100	10.663	8
Fe xxiii	$10.96^{+0.06}_{-0.04}$	0.069	10.981	12
Fe xvii	$11.26^{+0.04}_{-0.13}$	0.100	11.254	12
Fe xxiv	11.49 ± 0.05	0.071	11.432	18
Fe xxii	12.0 ± 0.2	0.100	11.977	9
Ne x (α)	$12.14^{+0.03}_{-0.04}$	0.059	12.132	26
Fe xxi	$12.34^{+0.06}_{-0.04}$	0.072	12.284	22
Fe xx	$12.531^{+0.1}_{-0.2}$	0.100	12.576	14
Fe xx	$13.1^{+0.6}_{-0.3}$	0.100	12.864	9
Ne ix (r)	$13.47^{+0.05}_{-0.03}$	0.067	13.447	25
Ne ix (f)	$13.68^{+0.04}_{-0.03}$	0.061	13.699	37
Fe xxi	$13.98^{+0.03}_{-0.02}$	0.053	14.008	34
Fe xviii	$14.17^{+0.03}_{-0.02}$	0.055	14.208	45
Fe xviii†	$14.31^{+0.03}_{-0.12}$	0.100	14.373	35
O viii	$14.82^{+0.05}_{-0.03}$	0.070	14.821	17
Fe xvii	$15.01^{+0.02}_{-0.04}$	0.060	15.014	37
Fe xix	$15.13^{+0.06}_{-0.04}$	0.081	15.079	33
Fe xvii	$15.44^{+0.04}_{-0.08}$	0.092	15.453	18
Fe xviii	$15.93^{+0.02}_{-0.03}$	0.057	15.931	25
Fe xviii	$16.05^{+0.04}_{-0.2}$	0.100	16.071	15
Fe xvi	$16.60^{+0.05}_{-0.03}$	0.072	16.567	29
Fe xvii	$16.70^{+0.04}_{-0.09}$	0.099	16.780	32
Fe xvii	17.03 ± 0.02	0.052	17.051	64
O vii	$18.65^{+0.2}_{-0.03}$	0.100	18.627	5
O viii (α)	18.93 ± 0.02	0.054	18.967	73
N vii	$19.88^{+0.05}_{-0.06}$	0.094	19.826	6
O vii (r)	$21.55^{+0.04}_{-0.03}$	0.079	21.602	6
O vii (i)	$21.82^{+0.06}_{-0.04}$	0.096	21.804	6
O vii (f)	$22.06^{+0.01}_{-0.02}$	0.059	22.098	56
Fe xxiv	$22.3^{+0.1}_{-0.2}$	0.100	22.249	6
N vii	$24.74^{+0.02}_{-0.01}$	0.067	24.779	97
N vii	$24.94^{+0.02}_{-0.04}$	0.078	24.898	34

Table 2. (1) the emission Line ID as determined by the highest probability transition within the search range given by AtomDB. (2) The wavelength detected by the Gaussian line profile, given in Angstroms. (3) The search range used to identify the lines, it was determined by the size of the uncertainty in wavelength placement plus a $z=0.002$ inflow/outflow allowance up to a maximum of 0.1 Å. (4) The rest wavelength as reported from AtomDB. (5) The fit improvement of including this line. (★) This line was fit independently of all others due to its close proximity of the Ne x line at 10.238 Å. (†) This line was initially frozen and then fit with all other lines free

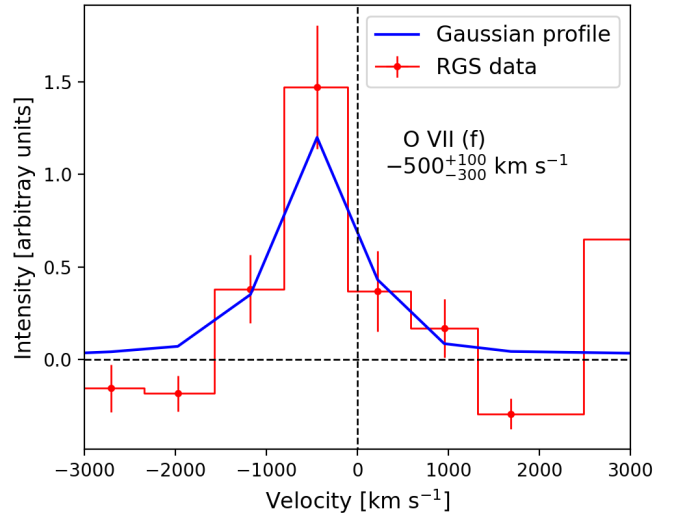


Figure 4. The velocity profile for the forbidden line of O VII with a Gaussian line overlaid. The forbidden O VII line is the strongest single feature in the RGS spectra, and thus is the best line candidate to explore the outflow velocity. Based on this line the outflow velocity is -500^{+100}_{-300} km s⁻¹.

see an incredibly strong forbidden line and weak intercombination and resonance lines. Assuming we are in the region where R is very sensitive to density (which was allowed by the calculated R ratio) than this is indicative to a photoionized plasma.

3.5 Neon Abundance

A neon overabundance was proposed in Grupe et al. (2004) to explain a feature they observed at 0.91 keV in the 5 ks PN data. The feature was attributed to the Ne ix triplet. They did not detect the O vii triplet located at ~ 0.56 keV leading them to conclude that there was an overabundance of Ne in Mrk 1239. Subsequent works have used this overabundance while fitting the X-ray spectra (see Jiang et al. 2021).

The analysis of Buhariwalla et al. (2020) suggested the excess emission at 0.91 keV was in fact due to a blend of emission lines including the Ne ix triplet and Fe-L emission lines. In Figure 5 a comparison between the RGS spectra and the EPIC PN spectra is made. Here we see both the RGS (in red) and PN spectra (in black) compared from 11 – 16 Å. Both spectra have been normalized by their mean in this region to ease the comparison.

The red RGS data points show a plethora of emission features while the black PN data show an excess emission between 0.85 and 1 keV, similar to what was seen in the original 2001 observation by Grupe et al. (2004). Even with the deep 2021 PN observation, the Ne ix emission lines remain unresolved. The RGS spectrum is required to resolve the Ne ix triplet and the surrounding features to state that the excess emission seen in this object at 0.91 keV is not due solely to the Ne ix triplet but instead it is a blend of many emission features in this region.

Furthermore the overabundance described by Grupe et al. (2004) was reliant on the non-detection of the O vii triplet in addition to the enhancement of the Ne ix line by Fe-L emission. In the bottom panel of Figure 3 we can clearly see the O vii present in our RGS spectra. The detection of the O vii triplet and the confirmation that the Ne ix triplet was being enhanced by surrounding emission lines shows a Ne overabundance is not needed in this source.

(1)	(2)	(3)	(4)	(5)
Model Component	Model Parameters	Short name	O VII	Ne IX
Resonance Line	Wavelength	λ_r	21.602 Å	13.447 Å
	Normalization	r	$= (i + i * R) / G^2$	$= (i + i * R) / G^2$
Intercombination Line	Wavelength	λ_i	21.804 Å	13.553 Å
	Normalization	i	10^{-5}	3×10^{-6}
Forbidden Line	Wavelength	λ_f	22.098 Å	13.699 Å
	Normalization	f	$= i$	$= i$
G		G	5^{+15}_{-3}	$1.5^{+3.5}_{-0.9}$
CONSTANT				
R		R	> 2.5	> 1
CONSTANT				
Outflow Velocity			$-500 \pm 200 \text{ km s}^{-1}$	$-300^{+800}_{-600} \text{ km s}^{-1}$
VMSHIFT				

Table 3. G and R diagnostic ratios for O VII and Ne IX. The model components are listed in column (1), the model parameters are listed in column (2) and their short form names used in the text are listed in column (3). The values for each parameter for the O VII and Ne IX triplets are given in columns (4) and (5), respectively.

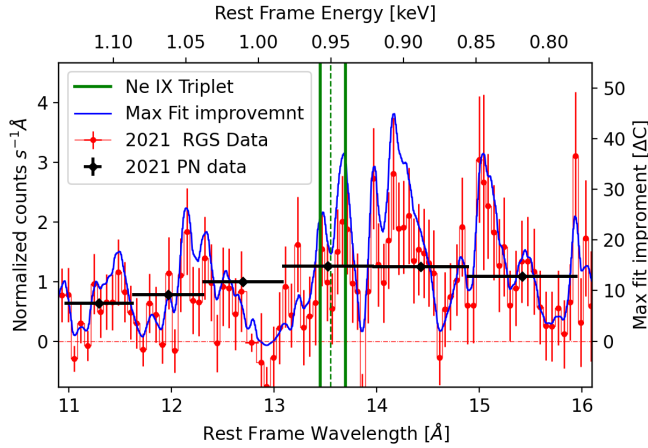


Figure 5. Comparison of the spectral resolution of the EPIC PN instrument to the RGS instrument. Red shows the RGS data, blue is the maximum fit improvement line (same as Figure 2) black denotes the PN data and green shows the location of the Ne IX triplet. The PN and RGS spectra have been normalized so that they may be presented on the same scale.

4 SPECTRAL MODELLING

The RGS data were background modelled in *XSPEC*, and C-statistics were used (Cash 1979) to evaluate the fit quality throughout. Errors were calculated at the 90 % confidence level using the *XSPEC* error command. Based on the results of the plasma diagnostics we proceeded with the assumption that there were at least two ionized regions present in the spectra.

We tested collisionally ionized plasma with *APEC*, version 3.0.9, (Smith et al. 2001) and a photoionized plasma using *XSTAR* grids, version 2.31 (Kallman & Bautista 2001). The model *MEKAL* (Liedahl et al. 1995) was tested in this analysis as it was what was originally used to model the data in Buhariwalla et al. (2020). Ultimately *APEC* was used as it contains more up to date atomic data, and produced better fit statistics. All fits were absorbed with a Galactic column density of $N_H = 4.43 \times 10^{20} \text{ atoms/cm}^2$ (Willingale et al. 2013).

XSTAR grids were calculated with a covering fraction of 1, luminosity of $10^{42} \text{ erg s}^{-1}$ and the turbulent velocity was fixed at 300

km s^{-1} . The ionizing continuum was described by a powerlaw with $\Gamma = 2.2$. The column density was logarithmically sampled at five points between 10^{20} and 10^{24} cm^{-2} . The density of the emitting material was logarithmically sampled at six points between 10^9 and 10^{14} cm^{-3} . The ionization parameter is defined as $\xi = L / nr^2$ (Tarter et al. 1969; Kallman & Bautista 2001) where L is the ionizing luminosity, n is the density of the material and r is the distance between the ionizing source and the emitting material. The log ionization was sampled linearly at 6 points between $\log \xi$ 1 and 4 erg cm s^{-1} . The column density, ionization and density were all interpolated for a total of a 300 step grid.

Seven subsequent grids were created with density at a fixed value ranging from 10^4 to 10^{10} cm^{-3} , $\log \xi$ was linearly samples at 10 points between 0 and 5, the column density was logarithmically sampled at ten points between 10^{20} and 10^{24} cm^{-2} . All other parameters were kept the same. These were 100 step grids. The 10^9 and 10^{10} cm^{-3} grids were tested against the 300 step grid for consistency, they produced the same fit statistic and ionization parameters. All abundances were fixed at solar.

For *APEC* the plasma temperature (kT) and normalization remained free, while the abundances remained fixed at solar. The powerlaw, when included, had free photon index and normalization.

Initially, emission from only one plasma component (*APEC* or *XSTAR*) was fitted to the RGS spectrum between 7–31 Å. With each individual plasma, the addition of a powerlaw component was considered to account for the underlying continuum. Fitting each of these components individually was able to account for select emission lines, but not all the emission features. The fits were $C/\text{dof} = 1319/814$ for *APEC* and $C/\text{dof} = 1360/813$ for *XSTAR*. The addition of a powerlaw (PO) component had fit improvements of $\Delta C = 22$ for *APEC*+PO for two additional free parameters. The addition of the powerlaw to *XSTAR* had a drastic fit improvement of $\Delta C = 83$ for two additional free parameters, but this was due to the poor initial fit of the *XSTAR* model *XSTAR*+PO results in a fit of $C/\text{dof} = 1277/811$.

Next two component plasmas were tested where both components were of the same type, this was done to explore the possibility of a single plasma with a gradient of temperature and/or ionization values. This produced slightly better fits than the addition of the powerlaw, with the fit improvement for *APEC*+*APEC* was $\Delta C = 27$ the single component counterpart, for two additional free parameters. *XSTAR*+*XSTAR*

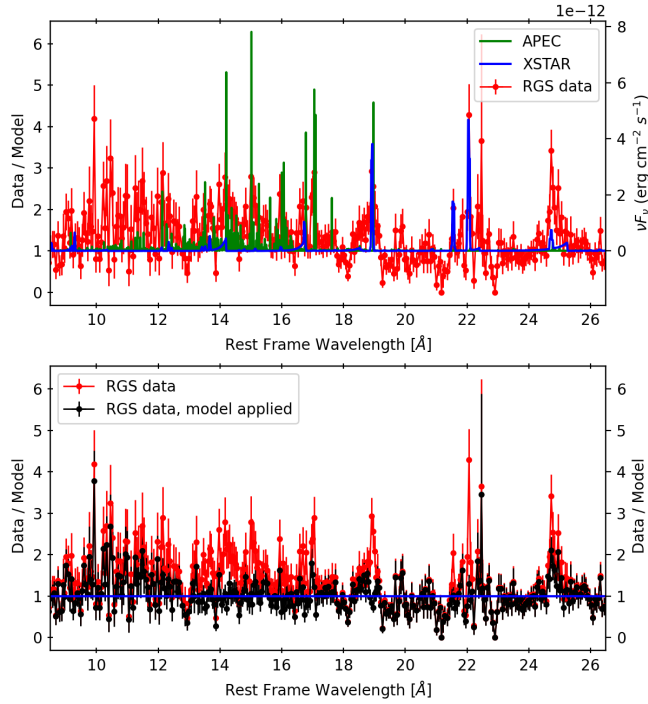


Figure 6. *Top panel:* the ratio of the RGS data and background model is shown in red, the fit here is $C/\text{dof} = 1716/816$. All data above ratio = 1 is above the background level. The best fit two component plasma is shown in green (APEC) and blue (XSTAR). The individual models are plotted to show which features are fit by each. *Bottom panel:* the red data are the same as above. The black data are the ratio of red data with the best fit model folded through the response ($C/\text{dof} = 1158/810$).

resulted in a fit improvement of $\Delta C = 69$, producing a worse fit than a single component+powerlaw model. Jiang et al. (2021) fit the soft band of Mrk 1239 with two collisionally ionized components. However their CCD spectra lacked the data quality to distinguish between a collisionally ionized and photoionized component.

4.1 Testing for Two Distinct Plasmas

A mixed plasma was tested such that it contained a collisionally ionized (APEC) and a photoionized (XSTAR) component. This produced a fit of $C/\text{dof} = 1201/811$. The APEC component produces a $\Delta C \sim 15$ better than the MEKAL component for the same degrees of freedom. The $\text{O VII}(f)$ line, which was outflowing with a velocity of $\sim -500 \text{ km s}^{-1}$, was produced by the photoionized plasma. Thus we test the $\text{XSTAR} + \text{APEC}$ models with the photoionized component allowed to outflow. The $\text{VMSHIFT} \times \text{XSTAR} + \text{APEC}$ model produces a superior fit of $C/\text{dof} = 1156/810$, $\Delta C = 45$ for one additional free parameter. Similar fit improvements were seen in the $\text{XSTAR} + \text{XSTAR}$ and $\text{APEC} + \text{APEC}$ fits when one component is allowed to outflow. No significant fit improvement were seen in these fits when both components are allowed to outflow. The best fit model can be found in Figure 6, the best fit parameters can be found in Table 4.1.

We can see that the photoionized material is outflowing with a velocity of $-660 \pm 150 \text{ km s}^{-1}$ which is consistent with the outflow velocity that we saw with $\text{O VII}(f)$ emission line. The density of the emitting material is $> 3.2 \times 10^{10} \text{ cm}^{-3}$, which is consistent with the density estimation found using the $\text{O VII } R$ ratio. The temperature of the emitting plasma is consistent with the temperature found in

(1)	(2)	(3)
Model Component	Model Parameter	Value
APEC	kT [keV]	$0.74^{+0.06}_{-0.07}$
	Abundance	1^f
XSTAR	Normalization [$\times 10^{-5}$]	3.8 ± 0.6
	Column density [cm^{-2}]	$< 2.5 \times 10^{22}$
	Log Ionization [erg cm s^{-1}]	$1.7^{+0.3}_{-0.2}$
	Density [cm^{-3}]	$> 3.2 \times 10^{10}$
	Redshift	0.01993^f
VMSHIFT	Normalization [$\times 10^{-6}$]	$2.6^{+0.5}_{-0.4}$
	Velocity [km/s]	-660 ± 150

Table 4. Best fit model parameters for the two component plasma model. Column (1) indicates the model component, Column (2) gives the Model Parameter and Column (3) gives the value of each parameter. All parameters with the superscript ‘f’ are kept fixed at quoted values.

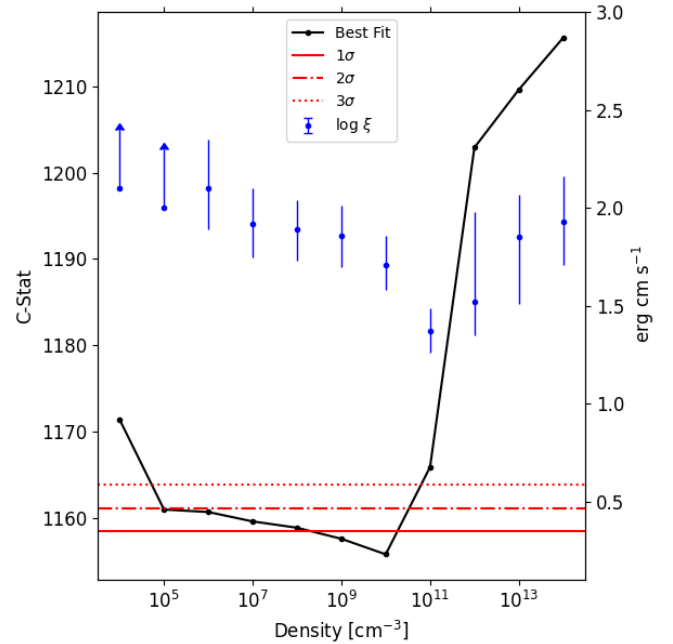


Figure 7. Density as a function of C-Stat (left axis) for the best fit two component plasma at different densities, and measured ionization at different density values (right axis).

Buhariwalla et al. (2020), despite the difference in model component (APEC vs MEKAL) and the difference in instrument (RGS vs MOS). There appears to be an excess of emission below 12 \AA and the $\sim 25 \text{ \AA}$ feature attributed to N VII appears under fit.

The best fit two component plasma gave an upper limit on density of less than $3.2 \times 10^{10} \text{ cm}^{-3}$, the XSTAR grid that gave this result was limited to densities above 10^9 cm^{-3} . Thus the lower limit of density was estimated using previously made grids with the same parameters. Figure 7 (left axis) shows the C-stat as a function of density, the minimum C-stat is 1156, given by the best fit model. 1, 2, and 3 σ lines are drawn to show the allowed density of the photoionized plasma. The allowed density is then between $10^5 - 10^{10} \text{ cm}^{-3}$. Ionization as a function of density (Figure 7 right axis) will be discussed in section 5.1.

XSTAR grids with ionizing continuum described by a powerlaw

with $\Gamma = 1.7$ and $\Gamma = 2.5$ were generated to test the effects of the continuum shape on the spectral appearance. They produced similar fit statistics as the best fit model, with $\Gamma = 2.2$. The measured properties of the *xstar* and *APEC* components were consistent, within error, to those quoted in Table 4.1. This led us to conclude that the shape of the continuum has a minimal effect on the properties of the photoionized emitter. This does not seem unreasonable in Mrk 1239 due to the modest data quality and small number of emission lines fit by the *xstar* component.

xstar grids with variable abundances were generated to explore the possibility of an overabundance in Mrk 1239. To ease computational time the density was fixed at 10^6 cm^{-3} and column density was fixed at 10^{23} cm^{-2} . All other parameters remained the same. Grids with variable Ne, O, Fe, and N were generated. Variable Ne and Fe had no effect on the fit of the RGS spectrum. Variable O and N produced best fit models with super solar ratios of N/O. The best fit grid produced a relative abundance of $N/O = 4 \pm 2 A_{\odot}$, with a $\Delta C = 16$. After investigation it was found that the driving mechanism for this super solar abundance is the 25 \AA N VII feature that was under fit in Figure 6. When the variable N grids are fit to the data below 25 \AA no overabundance or fit improvement is found. However when the data above 25 \AA was included the overabundance is present. Mao et al. (2019) showed that the relative N/O abundance could be super-solar in the ICM due to enrichment from low and intermediate mass stars. Their measured N/O agree with the value found here. However it is not immediately clear if this enrichment effect could also be present in the photoionized material of Mrk 1239, or if some other processes is driving the excess emission at 25 \AA .

The model under fits the data below 12 \AA , and no combination of collisionally or photoionized plasma could sufficiently fit the data in this region. This excess emission is also seen in the PN spectrum from this observation (Buhariwalla et al. in prep.) indicating that the excess emission is probably not from statistical fluctuations. Instead it may be that the AGN continuum in Mrk 1239 is becoming visible at wavelengths less than 12 \AA (energies greater than 1 keV). The RGS data are insufficient to make any inferences about the continuum. Thus this feature will be followed up in the future work on Mrk 1239 and its broadband spectra.

5 DISCUSSION

5.1 The Origin of the Photoionized Plasma

To explore the origin of the photoionized emitter we examined properties that could result in the measured ionization parameter. Recall the definition of the ionization parameter $\xi = L/nr^2$ (see Sec. 4). This can be rearranged as $r(n) = \sqrt{L/n\xi}$, allowing us to plot distance as a function of density. The ionization parameter (ξ) is degenerate with the density of the emitting material. This degeneracy is mitigated with the use of multiple *xstar* grids generated at different plasma densities. The right panel (right axis) of Figure 8 shows $\log \xi$ as a function of density.

The ionizing luminosity (L) was estimated using the models in Buhariwalla et al. (2020), however due to the uncertainty in the location of the emission material it is undetermined if the photoionized emitter sees the absorbed or unabsorbed luminosity, thus both luminosities are tested. Although the shape of the ionizing continuum would change between the absorbed and unabsorbed scenarios we showed in Section 4 where dramatic changes in the continuum have a minimal effect on the properties of the photoionized emitter. Thus for this exercise both luminosities can be used to estimate the properties of the photoionized emitter. We caution that the solution for

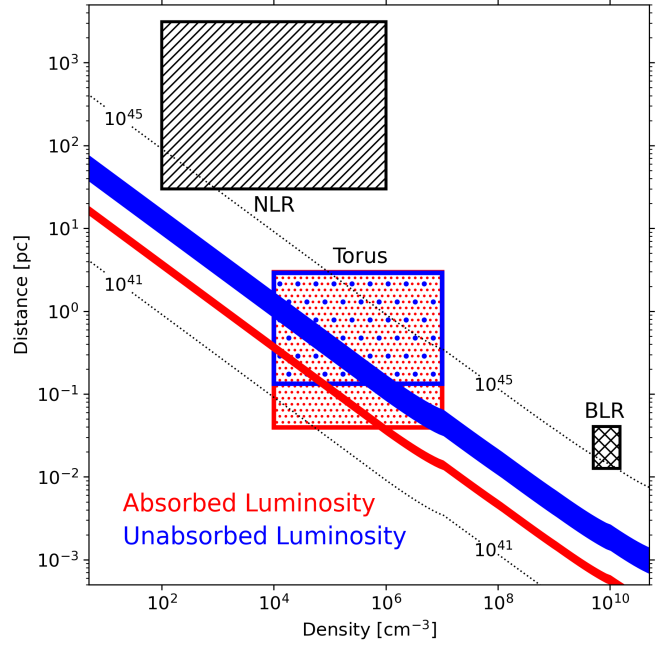


Figure 8. Density as a function of distance outlining the density-distance combinations that would produce the correct ionization for a given luminosity. The boxes outline the density-distance combinations for known components in AGN, they include the narrow line region (NLR), the broad line region (BLR) and the torus. See Section 5.1 for further details.

the unabsorbed luminosity is to be taken as approximate, as we did not re-run the models using the absorbed continuum to illuminate the emitting gas at all densities. A single *xstar* grid with density 10^{10} cm^{-3} was constructed using an absorbed ionizing continuum based on the absorbed continuum from Buhariwalla et al. (2020). It produced an ionization parameter greater than the unabsorbed scenario, however the difference was small on the distance-density plot. It resulted in a slight shift downward of the allowed regions for the absorbed luminosity.

The blue band in Figure 8 (left panel) shows where allowed combinations of distance and density lie for an unabsorbed source. The red band shows the same for an absorbed source. The variable ξ has some influence on the $r(n)$ plot, causing a small wave-like effect on the bands in Figure 8. To illustrate what kind of material would be able to produce these emission lines density and distance combinations of known AGN components are drawn in this plane.

The outer radius of the NLR was estimated using a $R_{\text{NLR}} - L_{[\text{O III}]}$ relationship derived for a sample of quasars and Seyfert galaxies (Bennert et al. 2002). The value of $\sim 3 \text{ kpc}$ is consistent with the radius of the extended NLR in Mrk 1239 found by Husemann et al. (2022). We take the inner radius of the NLR to be 30 pc , obtained from multi-density photoionization modelling of the NLR of Seyfert galaxies that reproduces a large range of NLR emission line intensities (Komossa & Schulz 1997). This is consistent with a sample of Seyfert 2s and intermediate Seyfert ($\sim \text{Sy}1.5$) galaxies (Vaona et al. 2012), and estimates using a second $R_{\text{NLR}} - L_{[\text{O III}]}$ relationship for the effective radius of the NLR in Seyfert galaxies given by Schmitt et al. (2003). For Mrk 1239, comparable values of $L_{[\text{O III}]}$ are given by Rafanelli & Bonoli (1984) and Malkan et al. (2017). The density is estimated measurements of intermediate Seyfert, and Seyfert 2 galaxies (Bennert et al. 2006; Vaona et al. 2012). We note that the

density and inner radius of the NLR may extend to lower values, but this provides a good order-of-magnitude estimate for our work.

The BLR size was estimated using $R_{\text{BLR}} = \lambda F_{\lambda}(5100 \text{ \AA})$ (Kaspi et al. 2005), with $\lambda F_{\lambda}(5100 \text{ \AA})$ for Mrk 1239 taken from Grupe et al. (2004) and Pan et al. (2021). The density of the BLR is given by Netzer (2013); Arav et al. (1998).

The outer radius of the torus in Mrk 1239 is measured to be 3 pc based on 12 μm observations (Tristram & Schartmann 2011). The inner torus radius (0.1–0.01 pc) is estimated by the dust sublimation radius with the luminosity estimated using models from Buhariwalla et al. (2020). The density of the torus is taken from Netzer (2013).

With all these components placed in the density - distance plane we begin to see what kind of material is producing the photoionized emission in Mrk 1239. A torus like structure produces the correct density - distance combination in both the absorbed and unabsorbed scenario. As discussed in section 4.1 the allowed density is between $10^5 - 10^{10} \text{ cm}^{-3}$, which agrees with a torus like structure again. The farthest allowed emitting region would be dependant on the lowest allowed density (10^5 cm^{-3}) and it would be at most a few pc, around the measured outer edge of the torus in Mrk 1239 (Tristram & Schartmann 2011).

If we analyse the full width half max (FWHM) of the $\text{O VII } (f)$ line we find that $\text{FWHM}_{\text{O VII } (f)} < 520 \text{ km s}^{-1}$. The Keplerian velocity of an object orbiting around the SMBH at the inner radius of the torus is $\sim 500 \text{ km s}^{-1}$. We can then conclude that the photoionized emitting material cannot be located any closer than the inner radius of the torus.

In summary, the RGS data have greatly increased our knowledge of the photoionized plasma in Mrk 1239, allowing us to determine its ionization, density and location. We now know that the material exists within several parsec of the central engine. Previous to these results it was not abundantly clear that there were emission line features in Mrk 1239, let alone to the extent detected here. However, several questions about the physical descriptions of the few parsec surrounding the central engine of Mrk 1239 remain. Namely, is this photoionized material related to the absorbing material we know is present in this source? Modelling the broadband X-ray continuum of Mrk 1239 requires heavy absorption from neutral and warm absorbers (Buhariwalla et al. 2020). It is easy to image that a large cloud could be illuminated by the central engine obscuring our line of sight to the central engine, while other regions of the cloud are photoionized, producing the photoionized spectra we see here.

Broadband analysis will shed some light onto the physical description of this region. For future X-ray telescope missions this exercise may be trivial. The top panel of Figure 9 shows a simulated *Athena-XIFU*³ 100 ks observation (Barret et al. 2022), using the best fit *xstar*+*APEC* model. Note that unlike with RGS, the *XIFU* spectrum is several orders of magnitude above the expected background. Most notably, *XIFU* data will distinguish between different ionizing continuum for the photoionized *xstar* grids. The data were simulated with an ionizing continuum of $\Gamma = 2.2$, equivalent to the continuum used for the majority of this work. The four grids fit to the *XIFU* data were ionized with: $\Gamma = 2.2$; $\Gamma = 2.5$; $\Gamma = 1.5$; and an empirical continuum based on the best fit absorbed continuum given by Buhariwalla et al. (2020). The ΔC value between the best fit $\Gamma = 2.2$ grid and the $\Gamma = 2.5$, $\Gamma = 1.5$, and absorbed continuum were $\Delta C = 391$, $\Delta C = 688$ and $\Delta C = 2476$, respectively. Thus with *XIFU* we easily

place restrictions on the ionizing continuum for the photoionized material. This is not even taking into account that *XIFU* will have high resolution spectroscopy up to $\sim 10 \text{ keV}$ allowing for direct testing of the link between the absorber and the photoionized emitter.

5.2 The Collisional Plasma in Mrk 1239

When testing spectral models no combination of photoionized emitters could fit the 13 – 17 \AA region well. Only the *APEC* and *MEKAL* models could adequately fit the data in this region. Figure 6 shows that this is the region of the RGS spectra that is dominated by the *APEC* component. The luminosity of each component was calculated using the *XSPEC* command *CLUMIN*. The *APEC* component had a luminosity of $L_{0.3-2.5 \text{ keV}} = 41.02^{+0.06}_{-0.07} \text{ erg s}^{-1}$, the *xstar* had $L_{0.3-2.5 \text{ keV}} = 41.05^{+0.06}_{-0.08} \text{ erg s}^{-1}$. The brightness of each feature was approximately equal.

Emission from Fe xvii at 16.777 \AA (3F), 17.050 \AA (3G), and 17.097 \AA (M2) are commonly seen in collisionally ionized plasma. The 3G and M2 lines are blended due to instrument resolution. They are often labelled $I(17.076 \text{ \AA})$ as they appear as one emission line feature at that wavelength. The O VII RRC is found at 16.769 \AA which blends with the 3F line much the same way 3G and M2 blend ($I(16.777 \text{ \AA})$). Phillips et al. (1997) measured the ratios of 3G/3F and M2/3F lines in the spectrum of the solar corona. Using their data the average value of ratio $(3F)/(3G + M2)$ was calculated to be 0.48 ± 0.2 . This suggests that if the ratio of $I(16.777 \text{ \AA})/I(17.076 \text{ \AA})$ is measured to be above 1 then than 50% of the flux in the $I(16.777 \text{ \AA})$ feature is contributed by the O VII RRC component.

Bianchi et al. (2010) found that the *APEC* model produced a ratio of ≈ 0.44 at varying plasma temperatures. They then measured the $I(16.777 \text{ \AA})/I(17.076 \text{ \AA})$ ratio in Mrk 573 to be $1.2^{+0.7}_{-0.5}$, concluding that the O VII RRC feature was contaminated by the 3F emission line. Similarly Marinucci et al. (2011) measured the ratio in NGC 424 to be $2.6^{+1.8}_{-1.9}$, and stated that the RRC component dominated over the Fe xvii lines. In Mrk 1239, the ratio is measured at $0.9^{+0.7}_{-0.4}$ indicating that both the Fe xvii emission and O VII RRC are contributing to $I(16.777 \text{ \AA})$.

Guainazzi & Bianchi (2007) studied obscured AGN (Sy 1.5 or greater) and found 16 of the 69 objects they investigated showed evidence of the O VII RRC feature. They took a ratio of 0.6 to indicate the RRC feature was dominate of the 3F emission line. Of those 16 galaxies, 15 had a ratio > 0.6 , and 13 were > 1.2 . Mrk 1239 ($0.9^{+0.7}_{-0.4}$) fits in the lower end of obscured AGN distribution and would be classified as having a dominate O VII RRC feature over the 3F line by Guainazzi & Bianchi (2007).

When the best-fit *xstar* model was applied to the data without the *APEC* component and the $(3F)/(3G + M2)$ ratio was measure it resulted in a value < 0.5 . This indicated that the photoionized emission was accounting for the O VII RRC feature and the remaining flux in this region was due to Fe xvii emission from collisionally ionized material.

Collisionally ionized emitters have been used to model the X-ray spectra of star forming regions in galaxies. Franceschini et al. (2003) approximated the SFR from the $L_{2-10 \text{ keV}}$ in ULIRGs without dominant AGN components. It is given by:

$$\text{SFR}_{\text{X-ray}}^{\text{ULIRG}} \approx \frac{L_{2-10 \text{ keV}}}{10^{39} \text{ erg s}^{-1}} \text{ M}_{\odot} \text{ yr}^{-1}. \quad (6)$$

Using just the *APEC* component allows us to estimate the non-AGN contribution of the 2–10 keV luminosity. We measure the *APEC* contribution to be $L_{2-10 \text{ keV}} \approx 3 \times 10^{39} \text{ erg s}^{-1}$, resulting in a SFR of

³ *XIFU* response files used were *XIFU_CC_BASELINECONF_2018_10_10*, retrieved from http://x-ifu-resources.irap.omp.eu/PUBLIC/RESPONSES/CC_CONFIGURATION/

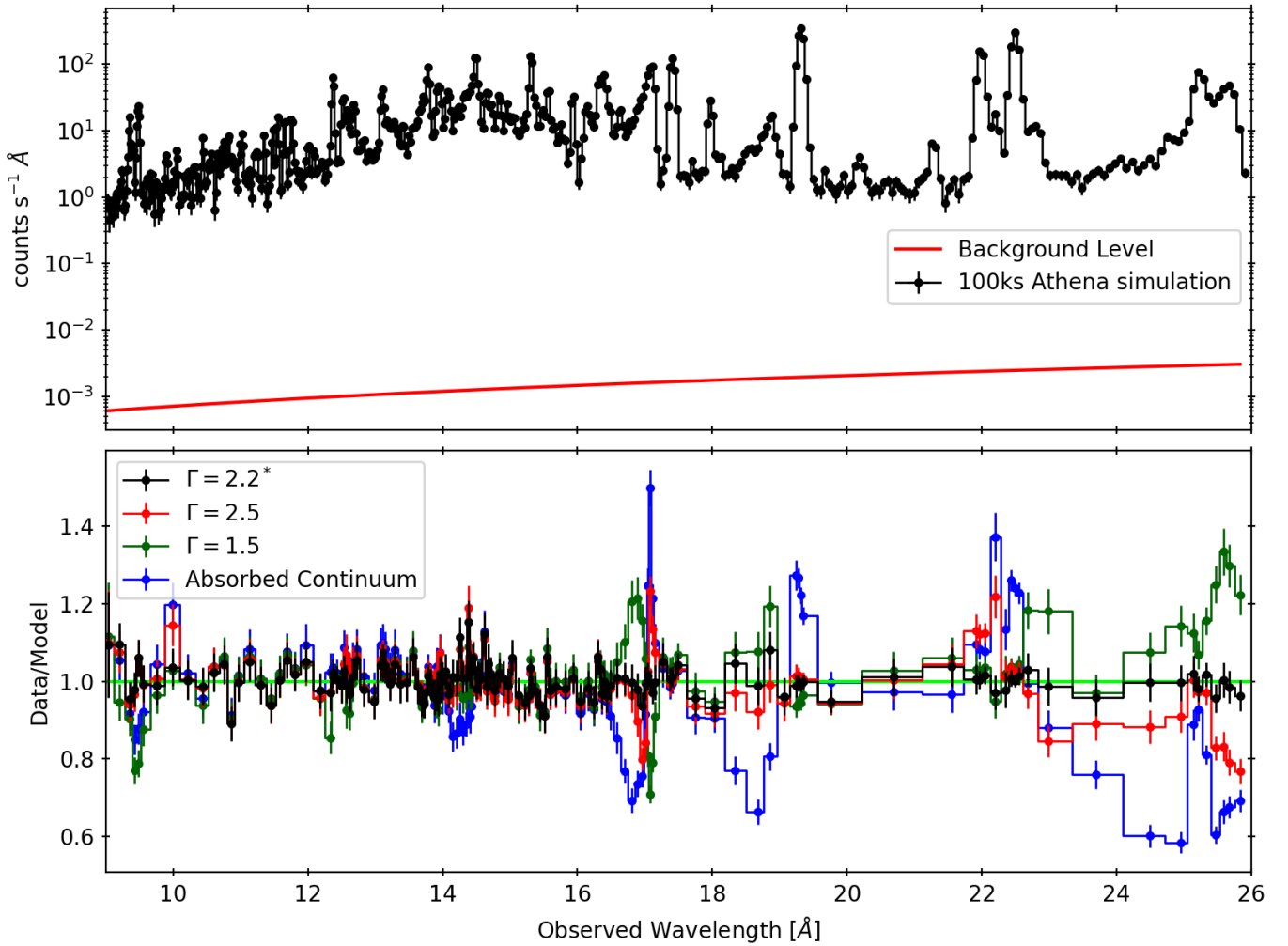


Figure 9. *Top panel:* 100 ks *Athena-XIFU* simulation with the best fit *xstar*+*APEC* model. The *xstar* grid was illuminated by a powerlaw continuum with $\Gamma = 2.2$. The approximate *XIFU* background is shown in red. *Bottom panel:* the *Athena* simulation fit with *APEC*+*xstar*, for four different *xstar* grids. The four grids have the same input parameter (covering fraction, luminosity, turbulent velocity, density, column density, ionization and abundances) but are illuminated by different ionizing continuum. The ionizing continuum are a mathematical powerlaw with $\Gamma = 2.2$, $\Gamma = 2.5$ and $\Gamma = 1.5$, as well as an empirical continuum model based on the absorbed continuum from the broad band spectra of Mrk 1239 (Buhariwalla et al. 2020). The ratios have been binned up for visual clarity.

$3 M_{\odot} \text{ yr}^{-1}$. This is consistent with previous measurements SFR in Mrk 1239 such as X-ray measurements ($3.7 - 5.8 M_{\odot} \text{ yr}^{-1}$; Buhariwalla et al. 2020), PAH measurements ($\lesssim 7.5 M_{\odot} \text{ yr}^{-1}$; Ruschel-Dutra et al. 2016), SED fitting ($3.47 \pm 0.26 M_{\odot} \text{ yr}^{-1}$; Gruppioni et al. 2016), and IR measurements ($2.1^{+0.5}_{-0.4} M_{\odot} \text{ yr}^{-1}$; Smirnova-Pinchukova et al. 2022). In the sample by Ruschel-Dutra et al. (2016), the luminosity from the collisionally ionized component matched those galaxies whose X-ray spectra were dominated by starburst component rather than those dominated by AGN.

5.3 Mrk 1239 Compared to Seyfert Galaxies

In a sample of 21 bright *ROSAT* selected AGN viewed with *XMM-Newton-EPIC*, only 2 of the galaxies studied preferred a soft excess with a line emitting region over a smooth blackbody (Gallo et al. 2006). The sample included 19 Seyfert galaxies (from Seyfert 1s to Seyfert 1.9s) and 2 LINERs and it was the two LINERs that required the CI component (MEKAL).

The RGS spectrum of Seyfert 1 galaxies is typically dominated by

features from photoionized plasma. This primarily includes emission from He-like ion triplets (e.g. O VII, Ne IX, N VI) and RRC features (O VIII, Ne IX, C VI). NGC 5548 is among the first Seyfert galaxies studied (Seyfert 1943), it possesses narrow and broad emission features in both the optical and X-ray bands (Cappi et al. 2016; Whewell et al. 2015). The RGS spectra of this object shows RRC features from Ne IX, O VII, O VIII, C V, and C VI. In addition the spectra show a strong O VII(*f*) line compared to the *i* and *r* lines. This galaxy shows strong evidence of several photoionized emitters and no evidence of any collisionally ionized material (Mao et al. 2018).

NGC 4151 is another well known Seyfert 1.5 galaxy. It shows many of the same features that NGC 5548 does including RRC and He-like triplets. The *R* and *G* ratios straddle the boarder between photoionized and collisional ionized plasma. However, the strength and shape of the RRC features in this galaxy point to a purely photoionized plasma (Armentrout et al. 2007).

The NLS1, Mrk 335 has been extensively studied with *XMM-Newton*. While early RGS spectra with low signal-to-noise supported a CI plasma (Grupe et al. 2008), these were not confirmed in later

works (e.g. Longinotti et al. 2013, 2019). Parker et al. (2019) examined the low continuum flux state when the emission lines were strongest and attributed them to photoionized emission.

Mrk 1239 shows strong evidence of collisionally ionized plasma, putting it at odds with the many of Seyfert 1 observations that favour photoionized emission. In Mrk 1239 the measured ratio of the forbidden O VII line to the O VII Ly α emission line is ≈ 1 as is expected for an obscured AGN (Sy 1.5 or greater) compared to the lower ratio for starburst galaxy (Guainazzi & Bianchi 2007).

NGC 1068 is a prototypical Seyfert 2 galaxy, and it shows a myriad of emission features stemming from multiple photoionized components. Based on visual inspection this galaxy has a spectrum that looks similar to Mrk 1239. The He-like triplets in NGC 1068 have similar appearances, with the Ne IX triplet showing equally strong *r* and *f* lines and no *i* line matching Mrk 1239 completely (Grafton-Waters et al. 2021). However the Ne IX triplet is not as blended with other lines in NGC 1068 as in Mrk 1239.

Original analysis of NGC 1068 showed that the maximum strength of a collisionally ionized plasma would be an order of magnitude less than the photoionized plasma (Kinkhabwala et al. 2002). However, the photoionization models used to describe the RGS spectrum failed to properly account for Fe XVII at 15 Å and 17 Å, thus Grafton-Waters et al. (2021) used a collisionally ionized component to model these lines. They stressed that this was most likely not caused by starburst activity. Instead it may be due to incomplete photoexcitation information in SPEX, causing PION to under predict emission in these lines. As for Mrk 1239 this does not seem to be the case as no matter the number of photoionized components applied (in addition to powerlaw components) the spectra is still under fit between 13 – 17 Å without the addition of APEC.

Mrk 1239 is a polar scattered Seyfert 1 galaxy, meaning our line of sight (LOS) passes through the upper layers of the torus polarizing the optical emission (Smith et al. 2004; Jiang et al. 2021). ESO 323-G77, another polar scattered Seyfert1, presents an X-ray spectra similar to Mrk 1239. This object shows high levels of variable absorption, that leave the soft band remarkably consistent below 1.5 keV (Mrk 1239 is consistent below 3 keV) and the harder bands show typical Seyfert variability (the same in Mrk 1239). In the soft band of ESO 323-G77 excess emission is seen at 0.9 keV, and can be modelled using a collisionally ionized plasma. This plasma has been interpreted as a region of star formation activity, and a SFR can be extracted in much the same way as is done here in Mrk 1239 (Miniutti et al. 2014).

ESO 323-G77 has been interpreted to be obscured by a clumpy torus, BLR clouds and a warm outflowing medium (Miniutti et al. 2014). The soft X-ray band of this object has been modelled using two APEC components, one with similar temperature to Mrk 1239 ($kT = 0.74$ keV), the other much cooler, $kT = 0.09$ keV. This is a difference in the modelling of these two objects, as the cool APEC component in ESO 323-G77 takes the place of a photoionized emitter. This cool APEC component fits a slight excess emission around ~ 0.5 keV, however it could be argued that the this excess emission could be originating from photoionized plasma (O VII triplet/N VII emission lines), but the CCD spectra lacks the resolution to distinguish between the components. Mrk 1239 could have a geometry similar to this object where the LOS is through the torus, creating a polarized BLR and absorbing the X-ray continuum, allowing for distant star forming regions to be visible in the soft X-ray band. ESO 323-G77 may exhibit a similar RGS spectrum as we have seen here in Mrk 1239.

If the soft X-ray band in Mrk 1239 is obscured in a similar manner as it is in ESO 323-G77, then an interesting avenue for analysis would be to investigate the connections with the photoionized emitter pro-

ducing the O VII triplet and the obscuring torus. Both sources would benefit from much deeper observations to explore this connection.

6 CONCLUSIONS

In this work we present the first deep RGS spectrum of Mrk 1239, it shows a myriad of ionized emission lines originating from a blend of photoionized and collisionally ionized plasma. The collisionally ionized plasma dominates the RGS spectra below 17 Å, while the photoionized plasma dominates above 17 Å. The O VII triplet is detected for the very first time in this source. Our main conclusions are as follows:

- i. Based on a strong 0.91 keV feature interpreted as Ne IX triplet and the lack of O VII triplet, Grupe et al. (2004) concluded that there was a super solar abundance of Ne/O. We show that the Ne IX triplet is enhanced in a CCD spectra by Fe-L transitions, as proposed by Buhariwalla et al. (2020), and that the O VII(*f*) triplet is present. All fits done in this work use a solar abundance of Ne/O, allowing us to conclude that Mrk 1239 does not have an over abundance of Ne.
- ii. Based on the line ratios of the O VII triplet and the variable density XSTAR grids, we can infer that the density of the photoionized material is between $10^5 - 10^{10} \text{ cm}^{-3}$. Using the definition of ionization and luminosities estimated from Buhariwalla et al. (2020) we can estimate that the photoionized emitter is located within a few pc of the SMBH. Based in on the FWHM of the O VII(*f*) emission line, the emitting material cannot be closer than the inner radius of the torus.
- iii. The collisionally ionized material is interpenetrated as a region of star forming activity. Based on relations from Franceschini et al. (2003) we estimate the SFR to be $\sim 3 M_{\odot} \text{ yr}^{-1}$. This is consistent with the SFR found by Buhariwalla et al. (2020) using the same method, and using PAH measurement of Mrk 1239 (Ruschel-Dutra et al. 2016).
- iv. Seyfert 1 galaxies typically show evidence of photoionized emission, it is uncommon for them to show evidence of collisionally ionized plasma in their X-ray spectra, placing Mrk 1239 in the minority along with ESO 323-G77.

The broadband spectrum Mrk 1239 will be presented in a future work. We will investigate any connection between the photoionized emitter and the highly absorbed continuum.

ACKNOWLEDGEMENTS

This work was based on observations obtained with XMM-Newton, an ESA science mission with instruments and contributions directly funded by ESA Member States and NASA. This research has also made use of data obtained from the Chandra Data Archive and the Chandra Source Catalog, and software provided by the Chandra X-ray Center (CXC) in the application packages CIAO and Sherpa. We thank the referee for comments that helped clarify the work. LCG acknowledges financial support from the Natural Sciences and Engineering Research Council of Canada (NSERC) and from the Canadian Space Agency (CSA). JJ acknowledges support from the Leverhulme Trust, Isaac Newton Trust, and St. Edmund's College University of Cambridge.

DATA AVAILABILITY

All data will be available through the HEASARC archive after the proprietary period has ended.

REFERENCES

- Arav N., Barlow T. A., Laor A., Sargent W. L. W., Blandford R. D., 1998, *MNRAS*, **297**, 990
- Armentrout B. K., Kraemer S. B., Turner T. J., 2007, *ApJ*, **665**, 237
- Barret D., et al., 2022, arXiv e-prints, [p. arXiv:2208.14562](https://arxiv.org/abs/2208.14562)
- Beers T. C., Kriessler J. R., Bird C. M., Huchra J. P., 1995, *AJ*, **109**, 874
- Bennert N., Falcke H., Schulz H., Wilson A. S., Wills B. J., 2002, *ApJ*, **574**, L105
- Bennert N., Jungwiert B., Komossa S., Haas M., Chini R., 2006, *A&A*, **456**, 953
- Bianchi S., Chiaberge M., Evans D. A., Guainazzi M., Baldi R. D., Matt G., Piconcelli E., 2010, *MNRAS*, **405**, 553
- Buhariwalla M. Z., Waddell S. G. H., Gallo L. C., Grupe D., Komossa S., 2020, *ApJ*, **901**, 118
- Capri M., et al., 2016, *A&A*, **592**, A27
- Cash W., 1979, *ApJ*, **228**, 939
- Doi A., Wajima K., Hagiwara Y., Inoue M., 2015, *ApJ*, **798**, L30
- Foord A., 2020, Dual AGN Across Cosmic Time, Chandra Proposal ID #22700153
- Franceschini A., et al., 2003, *MNRAS*, **343**, 1181
- Gallo L., 2018, *PoS*, NLS1-2018, 034
- Gallo L. C., Lehmann I., Pietsch W., Boller T., Brinkmann W., Friedrich P., Grupe D., 2006, *MNRAS*, **365**, 688
- Goodrich R. W., 1989, *ApJ*, **342**, 224
- Grafton-Waters S., Branduardi-Raymont G., Mehdipour M., Page M., Bianchi S., Behar E., Symeonidis M., 2021, *A&A*, **649**, A162
- Grupe D., Mathur S., Komossa S., 2004, *AJ*, **127**, 3161
- Grupe D., Komossa S., Gallo L. C., Fabian A. C., Larsson J., Pradhan A. K., Xu D., Miniutti G., 2008, *The Astrophysical Journal*, **681**, 982
- Gruppioni C., et al., 2016, *MNRAS*, **458**, 4297
- Guainazzi M., Bianchi S., 2007, *MNRAS*, **374**, 1290
- Husemann B., et al., 2022, *A&A*, **659**, A124
- Jansen F., et al., 2001, *AAP*, **365**, L1
- Järvelä E., Dahale R., Crepaldi L., Berton M., Congiu E., Antonucci R., 2022, *A&A*, **658**, A12
- Jiang J., et al., 2019, *MNRAS*, **489**, 3436
- Jiang J., Baloković M., Brightman M., Liu H., Harrison F. A., Lansbury G. B., 2021, *MNRAS*, **505**, 702
- Kastra J. S., Bleeker J. A. M., 2016, *AAP*, **587**, A151
- Kallman T., Bautista M., 2001, *ApJS*, **133**, 221
- Kaspi S., Maoz D., Netzer H., Peterson B. M., Vestergaard M., Jannuzi B. T., 2005, *ApJ*, **629**, 61
- Kinkhabwala A., et al., 2002, *ApJ*, **575**, 732
- Komossa S., 2008, in *Rev. Mex. Astron. Astrofis. Conference Series*, pp 86–92 ([arXiv:0710.3326](https://arxiv.org/abs/0710.3326))
- Komossa S., Schulz H., 1997, *A&A*, **323**, 31
- Liedahl D. A., Osterheld A. L., Goldstein W. H., 1995, *ApJ*, **438**, L115
- Longinotti A. L., et al., 2013, *ApJ*, **766**, 104
- Longinotti A. L., et al., 2019, *ApJ*, **875**, 150
- Malkan M. A., Jensen L. D., Rodriguez D. R., Spinoglio L., Rush B., 2017, *ApJ*, **846**, 102
- Mao J., et al., 2018, *A&A*, **612**, A18
- Mao J., et al., 2019, *A&A*, **621**, A9
- Marinucci A., Bianchi S., Matt G., Fabian A. C., Iwasawa K., Miniutti G., Piconcelli E., 2011, *A&A*, **526**, A36
- Miniutti G., et al., 2014, *MNRAS*, **437**, 1776
- Netzer H., 2013, *The Physics and Evolution of Active Galactic Nuclei*. Cambridge University Press, <https://search.ebscohost.com/login.aspx?direct=true&db=nlebk&AN=527870&site=ehost-live>
- Osterbrock D. E., Pogge R. W., 1985, *ApJ*, **297**, 166
- Pan X., et al., 2019, *ApJ*, **870**, 75
- Pan X., et al., 2021, *ApJ*, **912**, 118
- Parker M. L., et al., 2019, *MNRAS*, **490**, 683
- Phillips K. J. H., Greer C. J., Bhatia A. K., Coffey I. H., Barnsley R., Keenan F. P., 1997, *A&A*, **324**, 381
- Porquet D., Dubau J., 2000, *A&AS*, **143**, 495
- Rafanelli P., Bonoli C., 1984, *A&A*, **131**, 186
- Ruschel-Dutra D., Rodríguez Espinosa J. M., González Martán O., Pastoriza M., Riffel R., 2016, *MNRAS*, **466**, 3353
- Rush B., Malkan M. A., 1996, *ApJ*, **456**, 466
- Schmitt H. R., Donley J. L., Antonucci R. R. J., Hutchings J. B., Kinney A. L., Pringle J. E., 2003, *ApJ*, **597**, 768
- Seyfert C. K., 1943, *ApJ*, **97**, 28
- Smirnova-Pinchukova I., et al., 2022, *A&A*, **659**, A125
- Smith R. K., Brickhouse N. S., Liedahl D. A., Raymond J. C., 2001, *ApJ*, **556**, L91
- Smith J. E., Robinson A., Alexander D. M., Young S., Axon D. J., Corbett E. A., 2004, *MNRAS*, **350**, 140
- Tarter C. B., Tucker W. H., Salpeter E. E., 1969, *ApJ*, **156**, 943
- Tristram K. R. W., Schartmann M., 2011, *A&A*, **531**, A99
- Vaona L., Ciroi S., Di Mille F., Cracco V., La Mura G., Rafanelli P., 2012, *MNRAS*, **427**, 1266
- Waddell S. G. H., Gallo L. C., 2020, *MNRAS*, **498**, 5207
- Waddell S. G. H., Gallo L. C., Gonzalez A. G., Tripathi S., Zoghbi A., 2019, *MNRAS*, **489**, 5398
- Whewell M., et al., 2015, *A&A*, **581**, A79
- Wilkins D. R., Gallo L. C., 2015, *MNRAS*, **449**, 129
- Wilkins D. R., Gallo L. C., Silva C. V., Costantini E., Brandt W. N., Kriss G. A., 2017, *MNRAS*, **471**, 4436
- Willingale R., Starling R. L. C., Beardmore A. P., Tanvir N. R., O'Brien P. T., 2013, *MNRAS*, **431**, 394

This paper has been typeset from a \LaTeX file prepared by the author.